ACS APPLIED MATERIALS & INTERFACES

Research Article

www.acsami.org

Highly Efficient FRET System Capable of Deep Photodynamic Therapy Established on X-ray Excited Mesoporous LaF_3:Tb Scintillating Nanoparticles

Yong'an Tang, Jun Hu,* Ahmed H. Elmenoufy, and Xiangliang Yang*

National Research Centre for Nanomedicine, College of Life Science and Technology, Huazhong University of Science and Technology, Wuhan, 430074, P. R. China

Supporting Information

ABSTRACT: Photodynamic therapy (PDT) for deep-seated tumor is largely impeded by the limited penetration depth of excitation light in tissue. X-ray is considered as an ideal energy source to activate photosensitizers (PSs) located deep within the body with the assistance of scintillating nanoparticles (ScNPs). However, the efficacy under this concept is not satisfying due to the low scintillating luminescence and weak energy transfer from ScNPs to PSs. Here, mesoporous LaF_3:Tb ScNPs were successfully synthesized by a facile hydrothermal process to act as PS carriers and X-ray energy transducers, owing to their good ionizing radiation stopping power and high luminescence efficiency. The formation mechanism of porous structure was elucidated in detail with classical crystallization theory. After a systematic investigation, LaF_3:Tb ScNPs with optimized scintillating luminescence were obtained for loading Rose Bengal (RB) to establish an efficient FRET system, owing to their excellent spectral match. The FRET efficiency between ScNPs and RB was calculated to be as high as 85%. Under irradiation, enhanced $^1O_2$ generation induced by LaF_3:Tb-RB nanocomposites via FRET process was detected. This LaF_3:Tb-RB FRET system shows great potential to be applied in X-ray stimulated PDT for deep-seated tumors in the future.

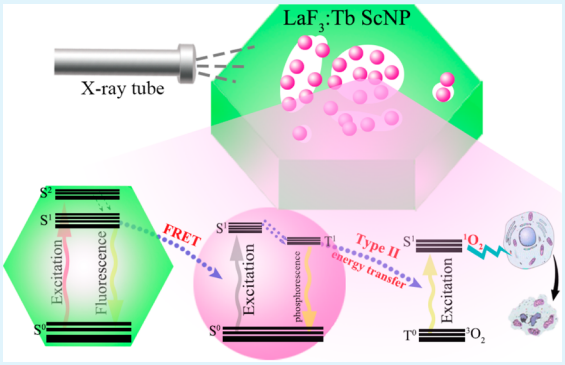

KEYWORDS: *scintillating nanoparticles, mesoporous, photodynamic therapy, FRET, X-ray, deep-seated tumor*

INTRODUCTION

Photodynamic therapy (PDT) is an emerging cancer therapy modality which contains three essential components: excitation light, photosensitizer (PS), and oxygen.[1] With the excitation of light at appropriate wavelength, PS is activated to produce reactive oxygen species (ROS) in the presence of oxygen molecules. In ROS, singlet oxygen ($^1O_2$) dominates the cytotoxicity of PDT via apoptotic, necrotic, and autophagy-associated pathways.[2] Compared with conventional therapy modalities, such as chemotherapy, surgery, and radiotherapy, the major advantages of PDT are the intrinsic safety, high selectivity, and minimal invasion.[3] Benefit from these characteristics, PDT has been extensively applied in clinic for cancer therapy.[4−8] However, the application of PDT is restricted to peripheral and endoscopically accessible regions due to the limited penetration depth of excitation light in tissue.[2,9,10]

In order to extend PDT to deep-seated tumors, NIR light, which possesses better tissue penetration ability, was introduced as the excitation source.[11−13] Several kinds of inorganic nanoparticles,[5] such as upconversion nanoparticles,[14−17] gold nanoparticles,[18−21] and quantum dots,[22] were employed to enhance the therapy efficacy. Although the light penetration depth can be improved to some extent under this concept, it is still limited to not more than 15 mm.[23] To thoroughly break through this remaining obstacle, X-ray was proposed as the energy source to initiate PDT, which can be named as X-ray excited PDT (XE-PDT).[24,25] Compared with conventional PDT modalities, XE-PDT exhibits many advantages. On the one hand, PDT for deep seated tumor therapy is accessible due to the unlimited penetration depth of the high-energy photons in tissue. On the other hand, utilization of X-ray as the PDT light source makes it feasible to integrate diagnosis, radiotherapy, and PDT for tumor theranostic applications. In this outstanding approach, not only can the tumor cure rate be raised, but the radiation dose and side effect in radiotherapy can be greatly diminished as well. Unfortunately, clinically used PSs have weak ability to absorb X-ray photons directly. To succeed in XE-PDT, antennas are usually employed to accept the energy of X-ray and then transfer it to PSs. Scintillating nanoparticles (ScNPs) are competent for this role due to their intense luminescence under X-ray irradiation.

XE-PDT based on scintillating nanoparticles was first proposed by Chen et al. in 2006,[25] and a lot of investigations in this field have been reported by his group.[26,27] Lanthanide-

Received: April 9, 2015
Accepted: May 14, 2015
Published: May 14, 2015

ACS Publications © 2015 American Chemical Society

DOI: 10.1021/acsami.5b03067
ACS Appl. Mater. Interfaces 2015, 7, 12261−12269

doped fluoride/oxide nanoparticles such as LaF_3:Tb/Ce or Tb_2O_3 were often used as X-ray energy acceptors. After the conjugation of commonly used PSs on the surface of these nanoparticles, $^1O_2$ could be generated under X-ray irradiation.[28] Compared with PSs alone, the amount of $^1O_2$ generated by ScNP-PS nanocomposites upon X-ray excitation was usually several times higher. Some researchers have observed cell damage and tumor inhibition of ScNP-PS nanocomposites with low-dose X-ray irradiation.[29−32] Although encouraging progress has been made after massive efforts, XE-PDT modality is still not as efficient as conventional PDT in terms of $^1O_2$ quantum yield, cancer cell killing efficiency, and tumor inhibition. After systematic summary and thorough analysis of the research progress, we conclude that the following reasons contribute to the unsatisfying results of XE-PDT: (a) In these works, ScNPs involved are usually lanthanide doped nanocrystals that many factors, including particle composition, crystal structure, and morphology are essential in the struggle for optimal luminescence efficiency. However, little attention has been paid to these parameters, not to mention the effects on X-ray luminescence and XE-PDT efficacy. (b) In XE-PDT, PSs are activated by photons emitted from ScNPs via FRET process in which energy transfer efficiency is greatly related to the spectrum overlap. In most of related works, PSs used are usually porphyrin or their derivatives which possess maximal absorption around 400 nm, while lanthanide-doped ScNPs often exhibit strong emission between 450 to 600 nm resulting in poor spectrum overlap,[26] weak energy transfer, and low XE-PDT efficacy. (c) The methods for the construction of ScNP-PSs nano/microcomposites are sometimes complicated and often involve tedious modification and conjugation procedures, during which the luminescence efficiency of scintillating particles and $^1O_2$ quantum yield of PSs will be largely attenuated.

For improving XE-PDT, mesoporous LaF_3:Tb nanoparticles with excellent scintillating luminescence were successfully prepared by a user-friendly and facile hydrothermal process. After a systematical investigation, the formation mechanism of mesopores was proposed and the effect of crystal composition, structure as well as morphology on X-ray luminescence of the ScNPs was clarified in detail. An optimized intense green luminescence corresponding to the $^5D_4 \rightarrow {}^7F_5$ transition of Tb^{3+} was observed under either UV light or X-ray irradiation. With a simple pore loading strategy, water-soluble PS molecules named Rose Bengal (RB) were encapsulated within LaF_3:Tb ScNPs to fabricate an efficient FRET system due to the exact overlap of ScNPs' emission band at 544 nm and RB's main absorption at 549 nm. Both steady-state spectra and fluorescence delay dynamic analysis demonstrated that FRET efficiency as high as 85% was achieved. Compared with RB alone, enhanced $^1O_2$ generation from LaF_3:Tb-RB nanocomposites was detected. All these results suggest that LaF_3:Tb-RB nanocomposites have great potential for deep PDT in the future.

EXPERIMENTAL SECTION

Chemicals and Synthesis. $LaCl_3{\cdot}7H_2O$, $TbCl_3{\cdot}6H_2O$, and NH_4F were all purchased from Aladdin Chemical Reagent Co. Ltd. 1,3-Diphenylisobenzofuran (DPBF) and Rose Bengal were bought from Sigma-Aldrich. All these chemicals were used as received without any treatment. LaF_3:Tb ScNPs were synthesized with a hydrothermal method. Typically, certain amount of $LaCl_3{\cdot}7H_2O$ and $TbCl_3{\cdot}6H_2O$ with different molar ratio was dissolved in deionized water. Under vigorously stirring, NH_4F with four times that amount of Ln^{3+} was dissolved in water and subsequently added dropwise by a pump within 30 min. The reaction was maintained for another hour after the completely adding of NH_4F. The gained solution containing nanoparticles were then transferred into a Teflon bottle held in a stainless steel autoclave and sealed. As the autoclave was cooled to room temperature naturally after the reaction, products were separated and washed by centrifugation. The obtained products were dried at 60 °C in oven overnight.

Characterization. Dynamic light scattering (DLS) measurements were done using Nanozs90 (Malvern, U.K.) instrument at a single scattering angle (90°). Wide-angle X-ray diffraction (XRD) measurements were carried out on a D8 Advance (Bruker, U.S.A.) X-ray diffractometer. The X-ray source was Cu Ka = 1.5418 Å and measurements were performed over the 2θ range 20° to 60° at a scanning rate of 6°/min. Transmission electron microscopy (TEM) images, high-resolution TEM (HRTEM) images, scanning electron microscope (SEM), and energy-dispersive X-ray spectroscopy (EDX) analysis of the nanocrystals were obtained with a Tecnai G2 F30 (FEI, Holland) transmission electron microscope. Inductively coupled plasma atomic emission spectrometry (ICP-AES) analysis was carried out using an Optima 4300DV (PerkinElmer, U.S.A.) ICP-AES to measure the Ln^{3+} ion concentration. Fluorescence spectra were acquired on F-4500 (Hitachi, Japan) fluorescence spectrometer. Fluorescent lifetime measurements were performed with excitation at 375 nm on a FLS 920 fluorescence system (Edinburgh Instruments, U.K.). Nitrogen adsorption−desorption isotherms were measured on a Micromeritics ASAP 2020 (Micromeritics Instrument, U.S.A.). The Brunauer−Emmett−Teller (BET) method was utilized to calculate the specific surface area. The pore-size distribution was derived using the Barrett−Joyner−Halanda (BJH) method. The X-ray excited luminescence spectra were measured on a homemade, named SicOmni-X, X-ray excited luminescence spectrometer, which is equipped with a F50−100 II tube (tungsten target, 75 kV, 20 mA) and Hamamatsu R92828 PMT (Shanghai Institute of Ceramics, Chinese Academy of Sciences). All measurements were carried out at room temperature.

RB Loading and $^1O_2$ Detection. LaF_3:Tb nanoparticles with a concentration of 10 mg/mL in deionized water were added with different amount of RB. After one-night stirring, the products were washed for several times and the emission spectrum and fluorescence lifetime were measured. DPBF was used to detect the generation of $^1O_2$. A certain amount of DPBF was mixed with LaF_3:Tb-RB nanocomposites. After different irradiation time, the fluorescence spectra of DPBF were recorded.

RESULTS AND DISCUSSION

Synthesis and Formation Mechanism for Mesoporous LaF_3:Tb ScNPs. Mesoporous LaF_3:Tb nanoparticles were prepared by a facile hydrothermal method in two steps. In the first step, the precursors Ln^{3+} and F^- reacted under vigorously stirring to form intermediates. In the second step, the intermediates were treated with high temperature and pressure to crystallize and mesopores were formed during this process. As can be seen from the SEM and TEM images in Figure 1, as-synthesized nanoparticles were uniform in size with regular hexagonal or sphere-like shapes and exhibited obvious porous structure. The size of the nanoparticles was calculated to be about 38.9 nm from TEM images and 70.2 nm from DLS measurements with a very low Polydispersity Index (PdI) value at 0.09 (Supporting Information, SI, Table S1), illustrating the high monodispersity of the products. As displayed in SI Figure S1, the hydrated size and polydispersity did not change within 24 weeks. In fact, after one-year storage under room temperature, no sediment or opacities were observed. Although no catalyst, surfactant, or template was used in this study during the synthesis procedure, the obtained nanoparticles exhibited wonderful water dispersibility and ultra colloidal stability. The

DOI: 10.1021/acsami.5b03067
ACS Appl. Mater. Interfaces 2015, 7, 12261−12269

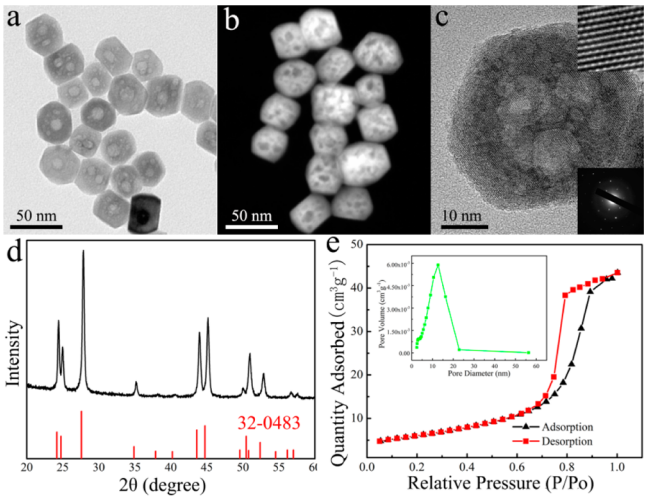

Figure 1. Characterization of mesoporous LaF_3:Tb ScNPs: (a) TEM image, (b) SEM image, (c) HRTEM image and SAED pattern, (d) XRD pattern, and (e) Nitrogen adsorption−desorption isotherms and pore-size distribution (insert) curve.

reason for this can be attributed to the existence of large number of unsaturated Ln^{3+} at the surface of the nanoparticles, making them positively charged and highly stable in water. As can be seen from the XPS analysis (SI Table S2), the molar ratio of F to Ln at the surface of the nanoparticles is much less than 3:1. This result indicates that there must be some dangling bonds of Ln^{3+} ions and part of them have coordinated with H_2O.

Sophisticated structural information on the mesoporous nanocrystal was acquired through HRTEM analysis, as it is shown in Figure 1c. Pores with different sizes were clearly seen and widely distributed. Distinct lattice fringe patterns were obvious even in the pore area, indicating the highly crystalline nature of the nanocrystals. Lattice spacing value was measured to be 0.32 nm (as shown in the top right corner), corresponding to *d*-spacing of (111) plane in hexagonal LaF_3. SAED pattern taken from a single particle (inset of Figure 1c at bottom right corner) implied the well-defined single-crystalline nature of the products. The positions of the XRD peaks were all in good agreement with the hexagonal phase structure of bulk LaF_3 crystals (JCPDS Card 32−0483), which was consistent with the results obtained from HRTEM analysis. The nanoparticles were composed with only La, Tb, and F, and the atomic ratio was exactly in agreement with the expected stoichiometry (SI Figure S2).

Nitrogen adsorption−desorption isotherms were employed to further investigate the nature of the porosity. The isotherm shown in Figure 1e was a typical type II curve, indicating the presence of mesopores proved by the hysteresis of the desorption. The BET surface area calculated from the curves was about 21.33 m^2/g. Barrett−Joyner−Halenda (BJH) analysis was applied to estimate the pore-size distribution, from which it could be seen that the pore size was mainly located in the region of several to a dozen nanometer, which was consistent with the TEM and SEM results. The unique mesoporous structure makes it possible for LaF_3:Tb scintillating nanoparticles to be ideal drug carriers through a facile pore encapsulation strategy.

In order to figure out the formation mechanism of mesoporous LaF_3:Tb nanoparticles, we studied the effects of hydrothermal temperature and reaction time on the size, morphology, and crystallization of the products. Figure 2 shows the typical TEM images and XRD patterns of LaF_3:Tb nanoparticles synthesized under a hydrothermal temperature at 200 °C with different duration time (0 h, 0.5 h, 1 h, 2 h, 4 h, 12 h, 72 h). From the TEM images, it was clear to see that the size and morphology changed significantly with the prolonged reaction time. Before hydrothermal treatment, the products were composed of large particles with diameters at 30 nm and small ones at 8 nm. When we took a careful insight into the larger ones with higher magnification, the particles were actually the aggregates of smaller nanocrystals. The coarse surface suggested a poor crystallinity, which was consistent with the low signal-to-noise ratio in XRD results, as shown in Figure 2b. After being treated with high temperature and high pressure for 1 h, small crystals disappeared. The particles became uniform, and small pores appeared. These results indicated that the small crystals aggregated and assembled to larger particles after a short hydrothermal time. Expending the reaction time to 2 h, the pores grew larger, and the shape of the particles changed from sphere to hexagon. Raising the reaction time to 4 h, the particles evolved completely to hexagon with uniform

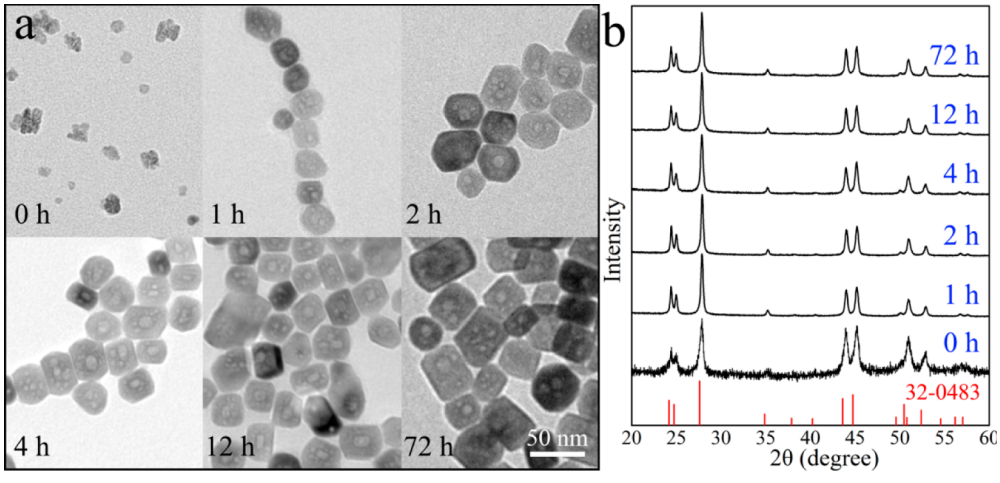

Figure 2. TEM images (a) and XRD patterns (b) of mesoporous LaF_3:Tb ScNPs synthesized at 200 °C with different duration time: 0 h, 1 h, 2 h, 4 h, 12 h, and 72 h.

DOI: 10.1021/acsami.5b03067
ACS Appl. Mater. Interfaces 2015, 7, 12261−12269

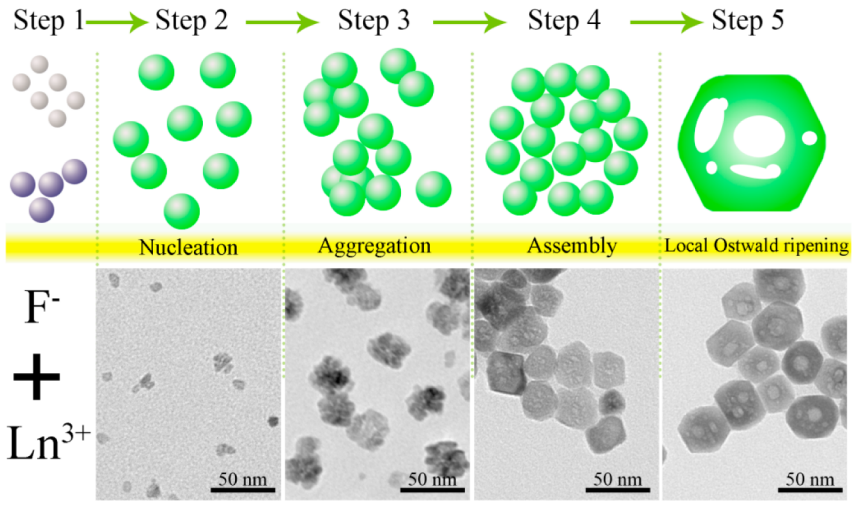

Figure 3. Evolution mechanism of mesoporous LaF_3:Tb ScNPs.

size. Further prolonging the hydrothermal reaction would not change the morphology of the nanoparticles any more except for the slight increase in size. As shown in SI Table S1, the particle size was increased from 25 nm before hydrothermal treatment to 45 nm after 72-h hydrothermal reaction. Increasing the hydrothermal temperature from 100 to 200 °C did not contribute much to the size and morphology of the nanoparticles, except for the increase of pore size (SI Figure S3).

On the basis of the experimental results obtained above, the formation mechanism of mesoporous LaF_3:Tb nanoparticles is proposed and illustrated in Figure 3. At the initial stage before hydrothermal treatment, massive small nuclei appeared owing to the reaction of Ln^{3+} and F^- precursors. With the addition of F^-, these nuclei, which possess high surface free energy were increasing more and more. For the purpose of lowering the total surface energy, they tended to accumulate to form irregular cluster-like aggregations without a preferential growth orientation as it can be seen from the TEM image in Step 3. It should be noted that the as-formed large particles did not show any crystallite coarsening. Treated with high temperature and high pressure, two adjacent small nuclei in these aggregative assemblies coalesced in the interface while the same crystallographic orientation appeared at the joint. This process was called self-recrystallization. Crystal fusion was restricted at the interface of mismatched lattices which gave rise to the generation of mesopores within the nanoparticles. Meanwhile, the aggregated nanocrystals underwent a local Ostwald ripening process, during which small crystals existed in the solution or at the edge of pores with relatively high surface energy dissolved and redeposited onto the surface of larger crystals resulting in the expansion of pores and gradual increase of particle size as well as the enhancement of crystallization. From the view of thermodynamics, the growth rate of the nanocrystals along each direction was different due to the difference of surface energy at each face, which eventually resulted in the formation of hexagon structure.

The mechanism of porous structure formation for lanthanide-doped nanoparticles has previously been reported by Wang and colleagues,[33] who synthesized mesoporous $NaTbF_4$ nanorice in the presence of ethylenediaminetetraacetic acid (EDTA). They attributed the pore formation to the effect of EDTA on the assembly behavior of small original crystals. However, as the results shown here, mesoporous nanoparticles can be obtained as well without EDTA. So we preferentially concluded that the formation of mesoporous structure under hydrothermal process was the intrinsic property of lanthanide ions but controlled by reaction parameters and doping component. In Wang's work, the nanopores were uniform in size (approximate 3−5 nm) and distributed homogeneously on the surface of particles, which was quite different from the results reported here. The pore size of our ScNPs was highly heterogeneous. The difference can be attributed to EDTA which served both as the chelating ligand to control the reaction rate and the capping agent to affect the facet growth and assembly behavior. Benefitting from the favor of EDTA, the crystals assemble regularly and only specific facet can fuse with other particles. The space between original crystals is restricted during the aggregation process. As a result, the nanopores formed are uniform in size and distributed homogeneously. Without EDTA, the original crystals are almost the same at any facet, so they will assemble and fuse with other particles around, randomly resulting in reduced restriction of space between crystals. With the favor of the minimization of interfacial energy, heterogeneous pores are formed. The widely distributed pores of our nanoparticles facilitate the loading of hydrophilic molecules, such as some organic dyes, antitumor drugs, as well as PSs.

The luminescence properties of the nanoparticles were measured at room temperature, as shown in Figure 4. The excitation spectrum was obtained by monitoring the emission of Tb^{3+} $^5D_4$−$^7F_5$ transition at 544 nm. The peaks were assigned to the transitions of electrons from $^7F_6$ ground state to different excited states within the $^4F_8$ configuration, 303 nm ($^5H_6$), 319 nm ($^5D_0$), 342 nm ($^5G_2$), 353 nm ($^5D_2$), 370 nm ($^5G_6$), and 375 nm ($^5D_3$), respectively.[34] Under the stimulation of UV light (375 nm) or X-ray, a prominent green emission band was observed at 544 nm along with three minor satellite peaks at 493, 588, and 622 nm. This typical emission of Tb^{3+} was due to the transitions between the excited $^5D_4$ state and the ^7F_J (J = 6−3) ground states. It was important to note that same spectrum was obtained under both UV and X-ray excitation modalities. Thus, UV light could be applied as excitation energy instead of X-ray in some research experiments. It is difficult to calculate the fluorescence quantum yield of the nanoparticles under the irradiation of X-ray. Therefore, we cannot compare

DOI: 10.1021/acsami.5b03067
ACS Appl. Mater. Interfaces 2015, 7, 12261−12269

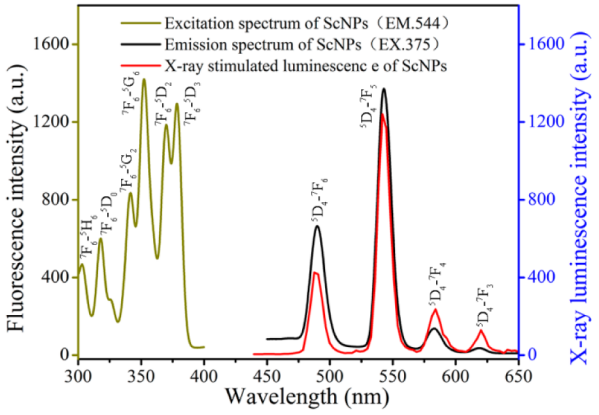

Figure 4. Luminescence properties of mesoporous LaF_3:Tb ScNPs.

the scintillating luminescence efficiency of our sample to that reported by other researchers. However, the X-ray-stimulated luminescence spectrum in our work exhibited relatively higher signal-to-noise ratio, and a smoother curve was obtained. Moreover, the mesoporous ScNPs showed rough resistance to photobleaching with less than 2% decrease of fluorescence intensity after 1-h continuous irradiation, as shown in SI Figure S4.

As mentioned above, the luminescence of LaF_3:Tb ScNPs was derived from Tb^{3+}. It is reasonable to recognize that the doping concentration of Tb^{3+} will affect the luminescence intensity of ScNPs. Samples with Tb^{3+} doping ratio varying from 0% to 100% (element concentration ratios are showed in SI Table S3) were prepared to investigate the effect of Tb^{3+} ratio on the synthesized particles. Typical TEM images and XRD patterns are displayed in Figure 5, from which it can be seen that the obtained nanoparticles changed from hexagon at low Tb^{3+} doping to sphere at middle doping and then to rod at high Tb^{3+} doping. Gradual increase of particle size was observed from both TEM and DLS analysis (SI Table S3). Porous abundance was obviously decreased with the increasing of Tb^{3+} doping concentration. The size of the pores was also reduced from 12 nm without Tb^{3+} doping to 4 nm with 60% Tb^{3+} doping. Changing in morphology might be attributed to effect of the crystal growth rate by Tb^{3+} doping through surface charge modification.[35] XRD analysis of the samples with Tb^{3+} doping lower than 60% was in good agreement with the pure hexagonal phase of LaF_3 (JCPDS 32-0483), except for the slight shifting of diffraction peaks to a larger angle along with the increase of doping ratio. The reason for the shifting was that more and more La^{3+} ions in the crystal lattice were replaced by Tb^{3+} which possesses a smaller ion radius, resulting in the reduction of unit-cell volume.[35] When increasing the Tb^{3+} doping ratio to higher than 60%, the crystal structure of the nanoparticles was gradually transformed from the hexagonal phase to an orthorhombic phase (as shown in SI Figure S5). The crystal phase also has a heavy influence on the scintillating luminescence of ScNPs. As it was reported by Kennedy and colleagues, the $NaGdF_4$:Eu nanoparticles with cubic crystal structure showed only half the fluorescence intensity of hexagonal crystals.[36]

Figure 5c shows the change of scintillating luminescence intensity of different Tb^{3+}-doped samples at 544 nm. Under the excitation of X-ray, the luminescence intensity had a sharp rise with the increasing of Tb^{3+} ratio at initial stage and reached the

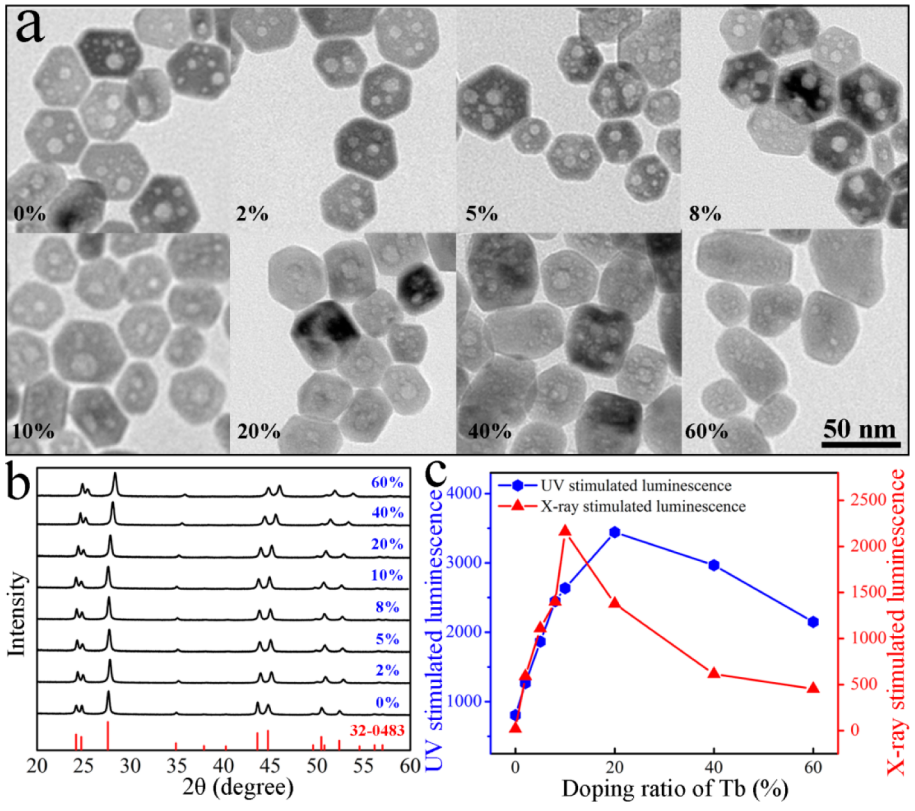

Figure 5. Characterizations of mesoporous LaF_3:Tb ScNPs with varied Tb^{3+} doping ratio (0%, 2%, 5%, 8%, 10%, 20%, 40%, and 60%): (a) TEM images, (b) corresponding XRD patterns, and (c) luminescence intensity at 544 nm under UV and X-ray stimulation.

DOI: 10.1021/acsami.5b03067
ACS Appl. Mater. Interfaces 2015, 7, 12261−12269

peak value at 10% Tb^{3+} doing. Beyond that, the luminescence intensity decreased with the addition of Tb^{3+}. Ion doping has multiple effects on luminescence behaviors. Specifically speaking, when the doping ratio was less than 10%, the concentration of luminescence centers rose with the increasing of Tb^{3+} doping and the distance between Tb^{3+} ions was getting closer which would result in less energy loss in excitons (electron−hole pairs) migration, leading to higher fluorescence intensity. On the contrary, continuously increasing Tb^{3+} doping ratio might cause self-quenching of Tb^{3+} activators, which was responsible for the decreased luminescence intensity at doping ratio between 10% and 60%. For UV light stimulated luminescence, the evolution of luminescence intensity at 544 nm was analogous to that under X-ray excitation. With the increasing Tb^{3+} doping ratio, the luminescence intensity of ScNPs had a sharp rise and then a slow decrease. The maximal value was achieved at 20% Tb^{3+} doping, which was a sharp contrast to the peak ratio of 10% under X-ray excitation. This discrepancy might be explained by the different luminescence mechanisms of LaF_3:Tb nanoparticles under these two excitation modalities. Therefore, the optimized scintillating luminescence could be obtained under 10% Tb^{3+} doping. Actually, different hydrothermal treatments also have a significant influence on the fluorescence intensity of ScNPs (as shown in SI Figure S3d and S6). It was found that the emission intensity increased with the hydrothermal temperature and treating time. The enhanced fluorescence can be contributed to the enhancement of crystallinity and the slight increase of the particle size.[37]

So far, a large number of lanthanide-doped oxide, phosphate, vanadate, and fluoride nano/microcrystals have been extensively studied as optical host matrix materials. Among which, LaF_3 has been proven to be one of the ideal host candidates owing to its special advantages, such as high resistivity, excellent thermal and environmental stability, and especially low vibrational energy.[38−40] These advantages will result in decreased quenching of activators and enhanced scintillating luminescence.

Construction of LaF_3:Tb-RB Nanocomposites for Deep PDT. To struggle for optimal XE-PDT efficacy, construction of proper ScNP-PSs FRET pairs with good spectrum overlap is a promising avenue to success. Owing to the porous structure of the synthesized LaF_3:Tb ScNPs, hydrophilic PSs could be simply loaded within the pores to establish a XE-PDT system. Here, RB was chosen as the PS based on the consideration of spectrum match and $^1O_2$ generation. RB is a water-soluble PS with $^1O_2$ quantum yield as high as 0.75.[41] And clinically, it is already used as a topical ophthalmic diagnostic agent without observable side-effects in humans.[42] Most importantly, the main absorption of RB at 549 nm overlaps exactly with the main emission band of LaF_3:Tb ScNPs at 544 nm, as shown in SI Figure S7. Actually, spectral overlap integral, $J(\lambda)$, can be calculated with the following formula:[43]

$$J(\lambda) = \frac{\int \mathrm{PL_D}(\lambda)\varepsilon_A(\lambda)\lambda^4 \, \mathrm{d}\lambda}{\int \mathrm{PL_D}(\lambda) \, \mathrm{d}\lambda}$$

where PL_D is the emission spectrum of the donor, ε_A is the absorption coefficient of the acceptor at the wavelength λ. And the $J(\lambda)$ value of LaF_3:Tb-RB is calculated to be 1.468×10^{-13} Mcm^{-1}, which means there is a good overlap between the emission of donor and the absorbance of acceptor. As LaF_3:Tb nanoparticles exhibit a similar emission spectrum under both UV and X-ray irradiation, efficient energy transfer will be expected in both excitation modalities.

As we know, assembly behavior has a heavy influence on the efficiency of FRET in XE-PDT, and several loading approaches such as covalent conjugation and physical loading have been employed.[26,44] In this study, the FRET system for XE-PDT was fabricated by a simple pore embedding method, as depicted in Scheme 1. In this way, tedious modification and conjugation

Scheme 1. Construction of Mesoporous LaF_3:Tb-RB Nanocomposites and Their Potential Application in Deep PDT

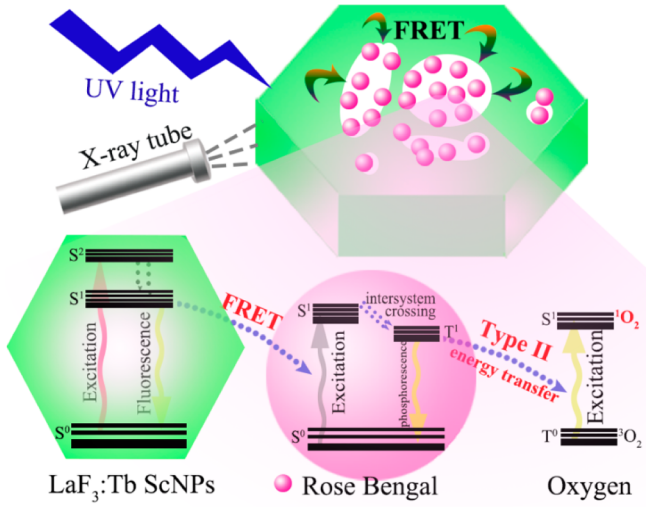

procedures are avoided. RB molecules are encapsulated inside the particles, resulting in closer distance between Tb^{3+} activators in crystals and RB in pores. In the FRET process, the efficiency is known to be distance dependent, which is proportional to the sixth power of the donor−acceptor distance.[45,46] Thus, this creative loading approach will contribute greatly toward acquiring high FRET efficiency.

After the loading of RB molecules, fluorescence spectra of LaF_3:Tb nanoparticles varied significantly, as shown in Figure 6a. The broad emission band of RB, which centered at 585 nm, was gradually enhanced at the expense of LaF_3:Tb emissions centered at 489 nm and 544 with increasing of RB concentration. The decrease of LaF_3:Tb emission and simultaneous increase of RB fluorescence indicated the presence of FRET between LaF_3:Tb nanoparticles and RB molecules. The FRET efficiency from donor to acceptor can be calculated according to the following equation:

$$E = 1 - \frac{F_D}{F_{DA}}$$

where F_D and F_{DA} are, respectively, the corresponding luminescence intensities of the donors in the presence and absence of the acceptor at the same donor concentration. Figure 6c depicted the FRET efficiency increased successively with the RB concentration. A FRET efficiency as high as 0.85 could be achieved, which indicated that RB molecules could be considered as efficient acceptors for LaF_3:Tb ScNPs.

The efficient energy transfer from LaF_3:Tb ScNPs to RB molecules can be further confirmed by time-resolved decay analysis. Luminescent dynamics of LaF_3:Tb at 544 nm was measured in the absence and presence of RB with different

DOI: 10.1021/acsami.5b03067
ACS Appl. Mater. Interfaces 2015, 7, 12261−12269

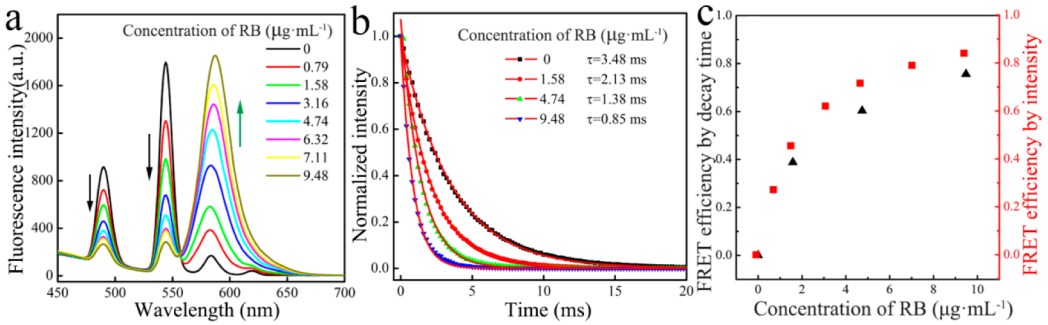

Figure 6. Fluorescence analysis of ScNP-PSs nanocomposites. (a) Successive change of emission spectra of LaF_3:Tb-RB FRET pair with the increasing of RB loading amount. (b) Fluorescence delay curves of LaF_3:Tb-RB nanocomposites monitored at 544 nm with difference RB concentration. (c) FRET efficiency as a function of RB concentration.

concentration. The obtained curves were fitted with a single exponential decay law and the results were displayed in Figure 6b. For LaF_3:Tb ScNPs without RB loading, the lifetime was calculated to be 3.48 ms. After the loading of RB, the lifetime of LaF_3:Tb at 544 nm was dramatically decreased with the increasing RB concentration. The results further demonstrated the occurrence of energy transfer from LaF_3:Tb to RB. Similar to fluorescence intensity, excited-state lifetime could be utilized to calculate the FRET efficiency,

$$E = 1 - \frac{\tau_D}{\tau_{DA}}$$

where τ_D and τ_{DA} are, respectively, the corresponding lifetime of donor in the presence and absence of acceptor. As it is shown in Figure 6c, the calculated FRET efficiency was close to the value obtained from the fluorescence intensity.

To further demonstrate the potential of utilizing the LaF_3:Tb-RB nanocomposites for PDT, $^1O_2$ generation was tested. DPBF is a commercial molecule probe for the detection of $^1O_2$ production. In the presence of $^1O_2$, DPBF was oxidized, accompanied by the quenching of fluorescence.[47] The fluorescence spectra of DPBF treated with LaF_3:Tb-RB nanocomposites after different irradiation time were recorded. It was found that the fluorescence intensity decreased gradually with the prolonging of irradiation time, indicating the continuous production of $^1O_2$. At the same time, control experiments were carried out to confirm whether the generation of $^1O_2$ was originated from direct activation of RB or via FRET process. Figure 7 shows the quenching of DPBF fluorescence by LaF_3:Tb ScNPs, RB and LaF_3:Tb-RB nanocomposites, respectively. The concentration of LaF_3:Tb ScNPs and RB was adjusted to be the same as the nanocomposites. RB alone could induce about 40% quenching of fluorescence due to the direct activation of RB, while the quenching induced by LaF_3:Tb-RB nanocomposites was found to be about two times higher than that by RB alone. LaF_3:Tb ScNPs alone nearly would not induce the generation of $^1O_2$. The results demonstrated that a high percentage of $^1O_2$ was produced via FRET process for LaF_3:Tb-RB nanocomposites. As we know, $^1O_2$ generation is the key point in photodynamic cancer therapy which can induce significant cell damage via apoptotic, necrotic, and autophagy-associated pathways.[2] Thus, enhanced PDT cytotoxicity can be expected when LaF_3:Tb-RB nanocomposites are applied in tumor treatment.

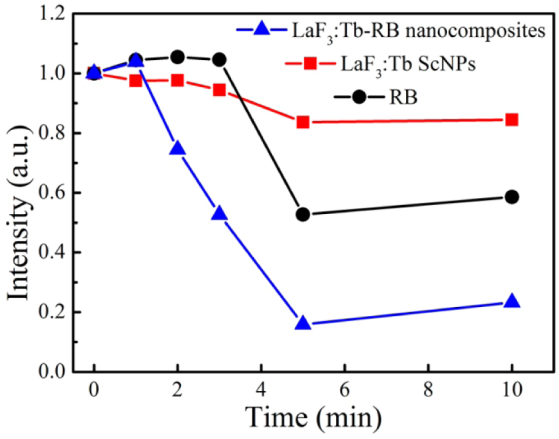

Figure 7. Decrease of emission intensity of DPBF treated with LaF_3:Tb ScNPs, RB, and LaF_3:Tb-RB nanocomposites, respectively, after different irradiation time.

CONCLUSIONS

In this work, mesoporous LaF_3:Tb scintillating nanoparticles were synthesized with a user-friendly and facile hydrothermal method. The formation of mesopores can be attributed to self-recrystallization and local Ostwald ripening based on the theory of classical thermodynamic. After a detailed investigation, it was found that crystal composition, structure, and morphology had a significant effect on the scintillating luminescence of the nanoparticles. The optimized ScNPs can emit strong green luminescence under both UV light and X-ray excitation. With a simple pore loading approach, Rose Bengal was encapsulated within ScNPs to establish a LaF_3:Tb-RB FRET system, which possesses several advantages including well definite nanostructure, optimized scintillating luminescence, admired spectrum overlap, simple drug loading approach, high FRET efficiency, good water solubility, and ultra colloidal stability. Under external irradiation, plenty of $^1O_2$ can be generated indicating the potential application of this smartly designed system in XE-PDT for deep-seated tumor treatment. More studies to validate the X-ray activated PDT effects of LaF_3:Tb-RB system are underway. It is believed that this system will provide a new avenue to succeed in deep PDT.

ASSOCIATED CONTENT

Supporting Information

The change of Z-average and polydispersity of LaF_3:Tb nanoparticles within 24 weeks under room temperature (Figure S1); energy dispersive X-ray spectrum of LaF_3:Tb ScNPs

DOI: 10.1021/acsami.5b03067
ACS Appl. Mater. Interfaces 2015, 7, 12261−12269

(Figure S2); TEM images, XRD patterns and fluorescence emission spectra of ScNPs synthesized under different hydrothermal temperature (Figure S3); relative fluorescence intensity of LaF_3:Tb nanoparticles with continuous irradiation (Figure S4); XRD patterns of LaF_3:Tb nanoparticles with 80% and 100% Tb^{3+} doping (Figure S5); emission spectra of LaF_3:Tb nanoparticles prepared with different hydrothermal treating time (Figure S6); the spectrum overlap between luminescence of LaF_3:Tb nanoparticles and absorption of RB (Figure S7); Z-average, polydispersity and size from TEM of LaF_3:Tb nanoparticles synthesized with different hydrothermal time (Table S1); element contents at the surface of LaF_3:Tb ScNPs obtained from XPS measurement (Table S2); Z-average, polydispersity, size from TEM and Tb ion ratio of LaF_3:Tb nanoparticles synthesized with different Tb doping (Table S3). The Supporting Information is available free of charge on the ACS Publications website at DOI: 10.1021/acsami.5b03067.

AUTHOR INFORMATION

Corresponding Authors

*Phone: 0086-27-87793539, Fax: 0086-27-87792234, E-mail: hjun0718@163.com (J.H.).

*Phone: 0086-27-87793539, Fax: 0086-27-87792234, E-mail: nanomedicine@mail.hust.edu.cn (X.Y.).

Notes

The authors declare no competing financial interest.

ACKNOWLEDGMENTS

This work was financially supported by a grant from National Basic Research Program of China (program 973, 2012CB932500) and National Science Foundation of China (Grant Nos. 81201193 and 81473171). We give thanks to the Analysis and Test Center of Huazhong University of Science & Technology for XRD, TEM, HTEM, EDX measurements, and Shanghai Institute of Ceramics of Chinese Academy of Sciences for X-ray stimulated luminescence characterization.

REFERENCES

(1) Dougherty, T. J.; Gomer, C. J.; Henderson, B. W.; Jori, G.; Kessel, D.; Korbelik, M.; Moan, J.; Peng, Q. Photodynamic Therapy. *J. Natl. Cancer Inst.* **1998**, *90* (12), 889−905.

(2) Agostinis, P.; Berg, K.; Cengel, K. A.; Foster, T. H.; Girotti, A. W.; Gollnick, S. O.; Hahn, S. M.; Hamblin, M. R.; Juzeniene, A.; Kessel, D.; Korbelik, M.; Moan, J.; Mroz, P.; Nowis, D.; Piette, J.; Wilson, B. C.; Golab, J. Photodynamic Therapy of Cancer: An Update. *Ca-Cancer J. Clin.* **2011**, *61* (4), 250−281.

(3) Lin, L.; Xiong, L.; Wen, Y.; Lei, S.; Deng, X.; Liu, Z.; Chen, W.; Miao, X. Active Targeting of Nano-Photosensitizer Delivery Systems for Photodynamic Therapy of Cancer Stem Cells. *J. Biomed. Nanotechnol.* **2015**, *11* (4), 531−554.

(4) Shanmugam, V.; Selvakumar, S.; Yeh, C. S. Near-Infrared Light-Responsive Nanomaterials in Cancer Therapeutics. *Chem. Soc. Rev.* **2014**, *43* (17), 6254−6287.

(5) Cheng, L.; Wang, C.; Feng, L.; Yang, K.; Liu, Z. Functional Nanomaterials for Phototherapies of Cancer. *Chem. Rev.* **2014**, *114* (21), 10869−10939.

(6) Shibu, E. S.; Hamada, M.; Murase, N.; Biju, V. Nanomaterials Formulations for Photothermal and Photodynamic Therapy of Cancer. *J. Photochem. Photobiol. C* **2013**, *15*, 53−72.

(7) Master, A.; Livingston, M.; Sen Gupta, A. Photodynamic Nanomedicine in the Treatment of Solid Tumors: Perspectives and Challenges. *J. Controlled Release* **2013**, *168* (1), 88−102.

(8) Brown, S. B.; Brown, E. A.; Walker, I. The Present and Future Role of Photodynamic Therapy in Cancer Treatment. *Lancet Oncol.* **2004**, *5* (8), 497−508.

(9) Weissleder, R. A Clearer Vision for in Vivo Imaging. *Nat. Biotechnol.* **2001**, *19* (4), 316−317.

(10) Ethirajan, M.; Chen, Y.; Joshi, P.; Pandey, R. K. The Role of Porphyrin Chemistry in Tumor Imaging and Photodynamic Therapy. *Chem. Soc. Rev.* **2011**, *40* (1), 340−362.

(11) Yuan, A.; Wu, J. H.; Tang, X. L.; Zhao, L. L.; Xu, F.; Hu, Y. Q. Application of Near-Infrared Dyes for Tumor Imaging, Photothermal, and Photodynamic Therapies. *J. Pharm. Sci.* **2013**, *102* (1), 6−28.

(12) Pawlicki, M.; Collins, H. A.; Denning, R. G.; Anderson, H. L. Two-Photon Absorption and the Design of Two-Photon Dyes. *Angew. Chem., Int. Ed.* **2009**, *48* (18), 3244−3266.

(13) Schmitt, J.; Heitz, V.; Sour, A.; Bolze, F.; Ftouni, H.; Nicoud, J.-F.; Flamigni, L.; Ventura, B. Diketopyrrolopyrrole-Porphyrin Conjugates with High Two-Photon Absorption and Singlet Oxygen Generation for Two-Photon Photodynamic Therapy. *Angew. Chem., Int. Ed.* **2015**, *54* (1), 169−173.

(14) Wang, C.; Tao, H.; Cheng, L.; Liu, Z. Near-Infrared Light Induced in Vivo Photodynamic Therapy of Cancer Based on Upconversion Nanoparticles. *Biomaterials* **2011**, *32* (26), 6145−6154.

(15) Lv, R.; Zhong, C.; Li, R.; Yang, P.; He, F.; Gai, S.; Hou, Z.; Yang, G.; Lin, J. Multifunctional Anticancer Platform for Multimodal Imaging and Visible Light Driven Photodynamic/Photothermal Therapy. *Chem. Mater.* **2015**, *27* (5), 1751−1763.

(16) Lucky, S. S.; Muhammad Idris, N.; Li, Z.; Huang, K.; Soo, K. C.; Zhang, Y. Titania Coated Upconversion Nanoparticles for Near-Infrared Light Triggered Photodynamic Therapy. *ACS Nano* **2015**, *9* (1), 191−205.

(17) Dou, Q. Q.; Rengaramchandran, A.; Selvan, S. T.; Paulmurugan, R.; Zhang, Y., Core-Shell Upconversion Nanoparticle-Semiconductor Heterostructures for Photodynamic Therapy. *Sci. Rep.* **2015**, *5*, doi:10.1038/srep08252.

(18) Seo, S. H.; Kim, B. M.; Joe, A.; Han, H. W.; Chen, X.; Cheng, Z.; Jang, E. S. NIR-Light-Induced Surface-Enhanced Raman Scattering for Detection and Photothermal/Photodynamic Therapy of Cancer Cells Using Methylene Blue-Embedded Gold Nanorod@SiO_2 Nanocomposites. *Biomaterials* **2014**, *35* (10), 3309−3318.

(19) Chen, N. T.; Tang, K. C.; Chung, M. F.; Cheng, S. H.; Huang, C. M.; Chu, C. H.; Chou, P. T.; Souris, J. S.; Chen, C. T.; Mou, C. Y.; Lo, L. W. Enhanced Plasmonic Resonance Energy Transfer in Mesoporous Silica-Encased Gold Nanorod for Two-Photon-Activated Photodynamic Therapy. *Theranostics* **2014**, *4* (8), 798−807.

(20) Vijayaraghavan, P.; Liu, C. H.; Vankayala, R.; Chiang, C. S.; Hwang, K. C. Designing Multi-Branched Gold Nanoechinus for NIR Light Activated Dual Modal Photodynamic and Photothermal Therapy in the Second Biological Window. *Adv. Mater.* **2014**, *26* (39), 6689−6695.

(21) Vankayala, R.; Huang, Y. K.; Kalluru, P.; Chiang, C. S.; Hwang, K. C. First Demonstration of Gold Nanorods-Mediated Photodynamic Therapeutic Destruction of Tumors Via Near Infra-Red Light Activation. *Small* **2014**, *10* (8), 1612−1622.

(22) Wang, J.; Zhang, Z.; Zha, S.; Zhu, Y.; Wu, P.; Ehrenberg, B.; Chen, J. Y. Carbon Nanodots Featuring Efficient FRET for Two-Photon Photodynamic Cancer Therapy with a Low fs Laser Power Density. *Biomaterials* **2014**, *35* (34), 9372−81.

(23) Tian, G.; Gu, Z.; Zhou, L.; Yin, W.; Liu, X.; Yan, L.; Jin, S.; Ren, W.; Xing, G.; Li, S.; Zhao, Y. Mn^{2+} Dopant-Controlled Synthesis of $NaYF_4$:Yb/Er Upconversion Nanoparticles for in Vivo Imaging and Drug Delivery. *Adv. Mater.* **2012**, *24* (9), 1226−1231.

(24) Chen, W. Nanoparticle Self-Lighting Photodynamic Therapy for Cancer Treatment. *J. Biomed. Nanotechnol.* **2008**, *4* (4), 369−376.

(25) Chen, W.; Zhang, J. Using Nanoparticles to Enable Simultaneous Radiation and Photodynamic Therapies for Cancer Treatment. *J. Nanosci. Nanotechnol.* **2006**, *6* (4), 1159−1166.

(26) Zou, X. J.; Yao, M. Z.; Ma, L.; Hossu, M.; Han, X. M.; Juzenas, P.; Chen, W. X-Ray-Induced Nanoparticle-Based Photodynamic Therapy of Cancer. *Nanomedicine* **2014**, *9* (15), 2339−2351.

(27) Ma, L.; Zou, X.; Chen, W. A New X-Ray Activated Nanoparticle Photosensitizer for Cancer Treatment. *J. Biomed. Nanotechnol.* **2014**, *10* (8), 1501−1508.

DOI: 10.1021/acsami.5b03067
ACS Appl. Mater. Interfaces 2015, 7, 12261−12269

(28) Liu, Y. F.; Chen, W.; Wang, S. P.; Joly, A. G. Investigation of Water-Soluble X-Ray Luminescence Nanoparticles for Photodynamic Activation. *Appl. Phys. Lett.* **2008**, *92* (4), 043901.
(29) Bulin, A. L.; Truillet, C.; Chouikrat, R.; Lux, F.; Frochot, C.; Amans, D.; Ledoux, G.; Tillement, O.; Perriat, P.; Barberi Heyob, M.; Dujardin, C. X-Ray-Induced Singlet Oxygen Activation with Nanoscintillator-Coupled Porphyrins. *J. Phys. Chem. C* **2013**, *117* (41), 21583−21589.
(30) Zhang, C.; Zhao, K.; Bu, W.; Ni, D.; Liu, Y.; Feng, J.; Shi, J. Marriage of Scintillator and Semiconductor for Synchronous Radiotherapy and Deep Photodynamic Therapy with Diminished Oxygen Dependence. *Angew. Chem., Int. Ed.* **2015**, *54* (6), 1770−1774.
(31) Chen, H.; Wang, G. D.; Chuang, Y.-J.; Zhen, Z.; Chen, X.; Biddinger, P.; Hao, Z.; Liu, F.; Shen, B.; Pan, Z.; Xie, J. Nanoscintillator-Mediated X-Ray Inducible Photodynamic Therapy for in Vivo Cancer Treatment. *Nano Lett.* **2015**, *15* (4), 2249−2256.
(32) Rossi, F.; Bedogni, E.; Bigi, F.; Rimoldi, T.; Cristofolini, L.; Pinelli, S.; Alinovi, R.; Negri, M.; Dhanabalan, S. C.; Attolini, G.; Fabbri, F.; Goldoni, M.; Mutti, A.; Benecchi, G.; Ghetti, C.; Iannotta, S.; Salviati, G., Porphyrin Conjugated SiC/SiO_x Nanowires for X-Ray-Excited Photodynamic Therapy. *Sci. Rep.* **2015**, *5*, doi:10.1038/srep07606.
(33) Chen, Z. M.; Geng, Z. R.; Shao, D. L.; Zhou, Z. P.; Wang, Z. L. Template-Free Synthesis of Mesoporous $NaTbF_4$ and $NaTbF_4$:Eu Nano-Rice and Their Luminescence Properties. *CrystEngComm* **2012**, *14* (6), 2251−2257.
(34) Li, S.; Zhang, X.; Hou, Z.; Cheng, Z.; Ma, P.; Lin, J. Enhanced Emission of Ultra-Small-Sized LaF_3:Re^{3+} (Re = Eu, Tb) Nanoparticles through 1,2,4,5-Benzenetetracarboxylic Acid Sensitization. *Nanoscale* **2012**, *4* (18), 5619−5626.
(35) Wang, F.; Han, Y.; Lim, C. S.; Lu, Y.; Wang, J.; Xu, J.; Chen, H.; Zhang, C.; Hong, M.; Liu, X. Simultaneous Phase and Size Control of Upconversion Nanocrystals through Lanthanide Doping. *Nature* **2010**, *463* (7284), 1061−1065.
(36) Sudheendra, L.; Das, G. K.; Li, C. Q.; Stark, D.; Cena, J.; Cherry, S.; Kennedy, I. M. $NaGdF_4$:Eu^{3+} Nanoparticles for Enhanced X-Ray Excited Optical Imaging. *Chem. Mater.* **2014**, *26* (5), 1881−1888.
(37) Sun, W.; Cui, X.; Wang, Z.; Wei, W.; Peng, B. Luminescence Properties of Nd^{3+}-Doped LaF_3 Nanocrystals with a Long Lifetime in Organic Solvents. *J. Mater. Chem.* **2012**, *22* (14), 6990−6993.
(38) Weber, M. J. Probabilities for Radiative and Nonradiative Decay of Er^{3+} in LaF_3. *Phys. Rev.* **1967**, *157* (2), 262−272.
(39) Wang, Z. L.; Quan, Z. W.; Jia, P. Y.; Lin, C. K.; Luo, Y.; Chen, Y.; Fang, J.; Zhou, W.; O'Connor, C. J.; Lin, J. A Facile Synthesis and Photoluminescent Properties of Redispersible CeF_3, CeF_3:Tb^{3+}, and CeF_3:Tb^{3+}/LaF_3 (Core/Shell) Nanoparticles. *Chem. Mater.* **2006**, *18* (8), 2030−2037.
(40) Zhang, Y. W.; Sun, X.; Si, R.; You, L. P.; Yan, C. H. Single-Crystalline and Monodisperse LaF_3 Triangular Nanoplates from a Single-Source Precursor. *J. Am. Chem. Soc.* **2005**, *127* (10), 3260−3261.
(41) Neckers, D. Rose Bengal. *J. Photochem. Photobiol., A* **1989**, *47* (1), 1−29.
(42) Wachter, E.; Dees, C.; Harkins, J.; Scott, T.; Petersen, M.; Rush, R. E.; Cada, A. Topical Rose Bengal: Pre-Clinical Evaluation of Pharmacokinetics and Safety. *Lasers Surg. Med.* **2003**, *32* (2), 101−110.
(43) Kar, A.; Kundu, A.; Bhattacharyya, S.; Mandal, S.; Patra, A. Lanthanide Based Resonance Energy Transfer (LRET) between Ce-Doped $LaPO_4$ Nanorods and Coumarin 440 Dye. *RSC Adv.* **2013**, *3* (32), 13372−13380.
(44) Abliz, E.; Collins, J. E.; Bell, H.; Tata, D. B. Novel Applications of Diagnostic X-Rays in Activating a Clinical Photodynamic Drug: Photofrin II through X-Ray Induced Visible Luminescence from "Rare-Earth" Formulated Particles. *J. X-Ray Sci. Technol.* **2011**, *19* (4), 521−530.
(45) Geißler, D.; Linden, S.; Liermann, K.; Wegner, K. D.; Charbonnière, L. J.; Hildebrandt, N. Lanthanides and Quantum Dots as Förster Resonance Energy Transfer Agents for Diagnostics and Cellular Imaging. *Inorg. Chem.* **2013**, *53* (4), 1824−1838.
(46) Forster, T. 10th Spiers Memorial Lecture. Transfer Mechanisms of Electronic Excitation. *Discuss. Faraday Soc.* **1959**, *27* (0), 7−17.
(47) Jin, S.; Zhou, L.; Gu, Z.; Tian, G.; Yan, L.; Ren, W.; Yin, W.; Liu, X.; Zhang, X.; Hu, Z.; Zhao, Y. A New Near Infrared Photosensitizing Nanoplatform Containing Blue-Emitting Up-Conversion Nanoparticles and Hypocrellin a for Photodynamic Therapy of Cancer Cells. *Nanoscale* **2013**, *5* (23), 11910−11918.

DOI: 10.1021/acsami.5b03067
ACS Appl. Mater. Interfaces 2015, 7, 12261−12269